ATLAS NOTE

ATLAS-CONF-2015-081

December 15, 2015

Search for resonances decaying to photon pairs in 3.2 fb^{-1} of pp collisions at $\sqrt{s}$ = 13 TeV with the ATLAS detector

The ATLAS Collaboration

Abstract

This note describes a search for new resonances decaying to two photons, with invariant mass larger than 200 GeV. The search is optimized for scalars such as those expected, for example, in models with an extended Higgs sector. The dataset consists of 3.2 fb^{-1} of pp collisions at $\sqrt{s}$ = 13 TeV recorded with the ATLAS detector at the Large Hadron Collider. The data are consistent with the expected background in most of the mass range. The most significant deviation in the observed diphoton invariant mass spectrum is found around 750 GeV, with a global significance of about 2 standard deviations. A limit is reported on the fiducial production cross section of a narrow scalar boson times its decay branching ratio into two photons, for masses ranging from 200 GeV to 1.7 TeV.

ATLAS-CONF-2015-081
15 December 2015

1 Introduction

One of the primary goals of the experiments at the Large Hadron Collider (LHC) is the search for new phenomena which might manifest themselves in the high-energy regime which is made accessible for the first time by this collider. This note reports on a search for new high-mass resonances in the diphoton channel using the dataset of proton-proton (pp) collisions recorded with the ATLAS detector [1, 2] at $\sqrt{s} = 13$ TeV in 2015. The integrated luminosity of this dataset is 3.2 fb^{-1}.

Using data recorded at $\sqrt{s} = 7$ TeV and $\sqrt{s} = 8$ TeV, the ATLAS and CMS collaborations have discovered a boson consistent with the Standard Model (SM) Higgs boson [3, 4] at a mass $m_H = 125.09 \pm 0.24$ GeV [5]. In models with an extended Higgs sector [6–12] new scalar resonances with masses larger or smaller than m_H are predicted. These resonances may be narrow when their branching ratio to two photons is non-negligible. A search in this final state benefits from a clean experimental signature with excellent mass resolution and limited background. Searches for new heavy scalars in the diphoton channel have been performed by the ATLAS and CMS collaborations using up to 20.3 fb^{-1} at $\sqrt{s} = 8$ TeV [13, 14].

This note reports an analysis optimized to search for Higgs-like resonances with mass larger than 200 GeV. The analysis selects pairs of photons using tight identification criteria to minimize backgrounds other than direct SM diphoton production. Additional Higgs-like resonances are expected to manifest themselves as localized excesses of events in the reconstructed diphoton invariant mass distribution over a large, smooth background. The background is parameterized by a smooth function with free parameters, which are adjusted to the data.

This note is organized as follows. Section 2 describes the experimental setup. Sections 3 and 4 respectively discuss the datasets used and the relevant simulated samples. Section 5 presents an overview of the reconstruction, calibration and identification of the photons used in the analysis. The optimization of the event selection is discussed in Section 6. Section 7 presents the signal and background modeling, while the statistical treatment is detailed in Section 8. Section 9 summarizes the systematic uncertainties affecting the analysis. The results and conclusions are respectively presented in Section 10 and 11.

2 Experimental setup

The ATLAS detector [1] at the LHC is a multi-purpose particle detector with a forward-backward symmetric cylindrical geometry and a near 4π coverage in solid angle[1]. It consists of an inner tracking detector surrounded by a thin superconducting solenoid providing a 2 T axial magnetic field, electromagnetic and hadron calorimeters, and a muon spectrometer. The inner tracking detector (ID) consists of silicon pixel, silicon micro-strip, and transition radiation tracking detectors. It provides precise track and vertex measurements in the pseudorapidity range $|\eta| < 2.5$. For the Run-2 of the LHC, a new pixel layer (Insertable B-Layer, IBL [2]) has been added at a radius of 33 mm. The electromagnetic (EM) calorimeter is a lead-liquid argon (LAr) sampling calorimeter with an accordion geometry, divided into a barrel section covering the pseudorapidity region $|\eta| < 1.45$ and two end-cap sections covering the

[1] ATLAS uses a right-handed coordinate system with its origin at the nominal interaction point (IP) in the center of the detector and the z-axis along the beam pipe. The x-axis points from the IP to the center of the LHC ring, and the y-axis points upwards. Cylindrical coordinates (r, ϕ) are used in the transverse plane, ϕ being the azimuthal angle around the z-axis. The pseudorapidity is defined in terms of the polar angle θ as $\eta = -\ln\tan(\theta/2)$. Angular distance is measured in $\Delta R \equiv \sqrt{(\Delta\eta)^2 + (\Delta\phi)^2}$.

pseudorapidity region $1.375 < |\eta| < 3.2$. The EM calorimeter has three longitudinal layers. The first one, with a thickness between 3 and 5 radiation lengths, has a high granularity in η (between 0.003 and 0.006 depending on η, 0.1 in ϕ, the regions $1.4 < |\eta| < 1.5$ and $|\eta| > 2.4$ are not covered), sufficient to provide discrimination between showers induced by single photons and by photon pairs from the decay of neutral mesons in jets. The second layer has a thickness of around 17 radiation lengths and a granularity of 0.025×0.025 in $\eta \times \phi$. A third layer, with a thickness varying between 4 and 15 radiation lengths, is used to correct for leakage beyond the EM calorimeter for high energy showers. In front of the calorimeter, a thin presampler layer, covering $|\eta| < 1.8$, is used to correct for fluctuations in upstream energy losses. The sampling term a of the energy resolution, $\sigma(E)/E \approx a/\sqrt{E\ (\text{GeV})} \oplus c$, varies between 9% and 14% as a function of $|\eta|$ for photons that do not convert into electron-positron pairs in the material upstream of the calorimeter (unconverted photons). For photons that do undergo such a conversion (converted photons), the sampling term a reaches a maximum of 20% near $|\eta| \sim 1.3$, where the material effect is largest. The sampling term is the largest contribution to the energy resolution up to about 100 GeV in photon transverse energy, where the constant term c starts to dominate (see Section 5 for details). In the region $|\eta| < 1.7$, the hadronic sampling calorimeter uses iron absorbers and plastic scintillator tiles as active material. The region $1.5 < |\eta| < 4.9$ is covered using LAr as active material with copper and/or tungsten absorbers. The muon spectrometer comprises separate trigger and high-precision tracking chambers, measuring the deflection of muons in a magnetic field generated by superconducting air-core toroids.

Events are selected using a first-level trigger implemented in custom electronics, which reduces the event rate to a design value of 100 kHz using a subset of detector information. Software algorithms with access to the full detector information (high-level trigger) are then used to yield a recorded event rate of about 1 kHz.

3 Data sample

Data were collected by the ATLAS detector in 2015 during pp collisions at a center-of-mass energy of $\sqrt{s} = 13$ TeV with bunch spacing of 25 ns, an average number of pp interactions per bunch crossing of about 13, and a peak instantaneous luminosity of $\mathcal{L} = 5.2 \cdot 10^{33}\ \text{cm}^{-2}\text{s}^{-1}$.

Events from pp collisions were recorded using a diphoton trigger with transverse energy E_{T} thresholds of 35 GeV and 25 GeV, for the E_{T}-ordered leading and subleading photon candidates respectively. In the high-level trigger, clusters of energy in the EM calorimeter are reconstructed and required to satisfy loose criteria according to expectations for EM showers initiated by photons. The trigger has a signal efficiency close to 99% for events fulfilling the final event selection.

Only events taken in stable beam conditions, and in which the trigger system, the tracking devices and the calorimeters were operational, are considered. After data-quality requirements, the data sample amounts to an integrated luminosity of $3.2\ \text{fb}^{-1}$.

4 Monte Carlo simulation

Simulated event samples are used to determine the shapes of the diphoton mass spectra for signal processes and to study the background parameterization. The simulation is used to correct the results from data for the selection inefficiencies and the detector resolution effects. Stable particles, defined as the particles with

lifetime of at least 10 ps, are passed through a full detector simulation [15] based on GEANT4 [16]. Pileup effects are simulated by overlaying each Monte Carlo (MC) event with a variable number of MC inelastic pp collisions generated using PYTHIA8 [17]. MC events are weighted to reproduce the distribution of the average number of interactions per bunch crossing observed in the data. The resulting detector simulation outputs are passed through the same event reconstruction algorithms as used for the data.

The signal is simulated using a SM Higgs-like boson produced in pp collisions at $\sqrt{s}$ = 13 TeV via gluon fusion (ggF), and decaying into two photons. MC samples are produced for different hypotheses of the scalar boson mass m_X, in the range [200 - 2000] GeV. The width of the simulated boson is set to 4 MeV, regardless of the resonance mass and corresponding to that of a 125 GeV SM Higgs boson. This choice will subsequently be referred to as the Narrow Width Approximation (NWA). The interference between the $gg \to X \to \gamma\gamma$ process, where X is the simulated scalar boson, and the QCD prompt diphoton production associated to the $gg \to \gamma\gamma$ process is estimated to be tiny and is therefore neglected in the simulation. The properties of the signal are also studied using the other main SM Higgs boson production modes: vector boson fusion (VBF), associated production with a vector boson (WH, ZH) and associated production with a top quark pair (ttH). Gluon-fusion events are generated with POWHEG-BOX [18, 19] interfaced with PYTHIA8 for the underlying event, parton showering and hadronization. VBF samples are generated using POWHEG-BOX [20] interfaced with PYTHIA8. WH, ZH and ttH samples are generated with PYTHIA8. The underlying event for the ggF and VBF samples, as well as the minimum-bias events, are simulated using the PYTHIA8 AZNLO tune [21], while the A14 tune [22] is used for all other signal samples. The CT10 [23] parton distribution function (PDF) set is used for the samples generated with POWHEG-BOX [18, 24, 25] while CTEQ6L1 [26] is used for the samples generated with PYTHIA8. The shape of the reconstructed invariant mass distribution of the NWA samples is completely dominated by detector effects, and in particular by the diphoton invariant mass resolution discussed in Section 5.

In addition to the NWA signal models, resonances with a natural width that cannot be neglected with respect to the experimental diphoton invariant mass resolution ("large" width) are studied. In order to obtain the mass distribution of a resonance with a large natural width, the convolution of a resolution function with a function parameterizing the resonance theoretical line shape is used, expanding the approach used in Run-1 by both ATLAS [13] and CMS [14]. The resolution function accounting for detector and reconstruction effects is obtained by fitting the reconstructed mass distributions of the NWA signal samples, since their response is completely dominated by detector effects[2]. A double-sided Crystal Ball function (DSCB) is used, defined as:

$$N \cdot \begin{cases} e^{-t^2/2} & \text{if } -\alpha_{\text{low}} \geq t \geq \alpha_{\text{high}} \\ \dfrac{e^{-\alpha_{\text{low}}^2/2}}{\left[\frac{\alpha_{\text{low}}}{n_{\text{low}}}\left(\frac{n_{\text{low}}}{\alpha_{\text{low}}} - \alpha_{\text{low}} - t\right)\right]^{n_{\text{low}}}} & \text{if } t < -\alpha_{\text{low}} \\ \dfrac{e^{-\alpha_{\text{high}}^2/2}}{\left[\frac{\alpha_{\text{high}}}{n_{\text{high}}}\left(\frac{n_{\text{high}}}{\alpha_{\text{high}}} - \alpha_{\text{high}} + t\right)\right]^{n_{\text{high}}}} & \text{if } t > \alpha_{\text{high}}, \end{cases} \tag{1}$$

where $t = \Delta m_X/\sigma_{\text{CB}}$, $\Delta m_X = m_X - \mu_{\text{CB}}$, N is a normalization parameter, μ_{CB} is the peak of the Gaussian distribution, σ_{CB} represents the width of the Gaussian part of the function, α_{low} (α_{high}) parameterizes the mass value where the distribution switches from a Gaussian to a power-law function on the low (high) mass side, and n_{low} (n_{high}) is the exponent of this power-law function. The theoretical line shape, as a function of the resonance mass m_X and of its natural width Γ, is chosen to be the POWHEG implementation of a large-width scalar resonance when assuming SM-like couplings [27]. The line-shape is modeled with

[2] The same fits are used to parameterize the NWA signal properties. See Section 7 for details.

a Breit-Wigner distribution with a mass-dependent width, including the dependence of the propagator on the gluon-gluon parton luminosity. In order to reduce modeling effects from the off-shell region, the sample generation is restricted to the region $m_X \pm 2\Gamma$. Large-width samples are produced in the mass range [200 - 2000] GeV for $\alpha = \Gamma/m_X$ ranging from 1% to 10%, in a width range where the interference with the continuous background is expected to be small [14]. Samples obtained with the above procedure for m_X = 400 GeV, 800 GeV and 1500 GeV, and α = 5%, 7% and 10% are compared with the corresponding fully-simulated Powheg samples, and found to be in very good agreement. More samples with α ranging from 10% to 25% are produced for validation purposes only.

Events containing two prompt photons produced by QCD processes, representing the largest irreducible background to the search, are simulated using the Sherpa [28] generator. Samples of the γ-jet reducible background component are also generated using Sherpa. The CT10 PDF set is used in conjunction with a dedicated parton-shower tune developed by the Sherpa authors.

The fixed-order NLO parton-level simulation provided by Diphox [29], to which a parametrized detector response is applied, is used to produce an alternative diphoton MC sample, including QCD NLO corrections and the contributions of the fragmentation process. Diphox 1.3.3 with the CT10 PDF set is used.

5 Photon reconstruction, calibration and identification

Photon reconstruction is seeded by clusters of EM calorimeter cells with transverse energies exceeding 2.5 GeV in projective towers of size 0.075×0.125 in $\eta \times \phi$, made from the presampler and the three EM calorimeter layers. The cluster reconstruction efficiency for photons and electrons with $E_{\mathrm{T}} > 25$ GeV is estimated from simulation to be close to 100% [30]. Clusters of cells in the EM calorimeters are then matched to tracks reconstructed in the ID and extrapolated to the calorimeter. Clusters matched to tracks are classified as electron candidates, while clusters without matching tracks are classified as unconverted photon candidates. Clusters matched to pairs of tracks that are consistent with the hypothesis of a $\gamma \to e^+e^-$ conversion process are classified as converted photon candidates. Clusters matched to single tracks without hits in an active region of the pixel layer nearest to the beam pipe are also classified as converted photon candidates. If no hit on the innermost layer is expected, the pixel layer next to it is considered. Some clusters are classified as both electron and photon candidates. The efficiency to correctly reconstruct photons from the clusters and tracks is 97%, while the remaining 3% are incorrectly reconstructed only as electron candidates. The probability for a primary electron with $E_{\mathrm{T}} > 25$ GeV to be reconstructed as a photon candidate fulfilling the tight identification criteria is measured in data to vary between 2% and 15%, depending on the pseudorapidity and whether the photon candidate is reconstructed as converted or unconverted.

The energy measurement is made in the electromagnetic calorimeter using a cluster size which depends on the photon position. A size of 0.075×0.175 in $\eta \times \phi$ is used for all candidates in the barrel EM calorimeter, in order to unify the cluster size for electrons, converted and unconverted photons[3]. In the end-cap EM calorimeter, a cluster size of 0.125×0.125 is used for all candidates. A dedicated energy calibration [31], updated for the Run-2 data-taking conditions, is applied to account for upstream energy losses, lateral and longitudinal leakage, separately for converted and unconverted photon candidates. The

[3] In Run-1, a size of 0.075×0.125 in $\eta \times \phi$ was used in barrel EM calorimeter for unconverted photon candidates, and 0.075×0.175 for converted photon candidates and electron candidates.

final energy calibration is determined from $Z \to e^+e^-$ events, resulting in η-dependent correction factors of the order of $\pm(1-3)\%$. An effective constant term for the calorimeter energy resolution is extracted by adjusting the width of the reconstructed Z mass distribution in simulation to match the distribution in data. The calibration factors are extracted from $Z \to e^+e^-$ events in 8 TeV data reconstructed with the 13 TeV reconstruction, and specific corrections accounting for the current detector conditions are applied. Additional systematic uncertainties on the energy scale and resolution are introduced to cover the different conditions between the Run-1 and Run-2 setups. After this calibration procedure, the constant term in the energy resolution is estimated to be (1.1±0.5)% in the barrel region of the EM calorimeter and (1.8±0.5)% in the end-cap region of the EM calorimeter. The energy resolution in the simulated samples is adjusted to match these values.

Photon candidates are required to fulfill identification criteria based on the shower shape in the electromagnetic calorimeter, and on energy leakage into the hadronic calorimeter [30]. A photon candidate is required to deposit only a small fraction of its energy in the hadronic calorimeter, and its transverse shower shape in the second layer of the EM calorimeter is required to be consistent with that expected from a single electromagnetic shower. The high-granularity first layer is used to further discriminate single photons from overlapping photon pairs originating from the decays of neutral mesons in jet fragmentation, which represent the main background source. A set of tight identification criteria has been optimized to match the running conditions and the ATLAS detector layout. In order to take into account small differences in shower shapes between data and simulation, a correction (shift) is applied to the variables describing the shape of the shower in the simulation. The shifts are taken from the Run-1 study, and verified to be compatible with the shifts observed between 2015 data and MC. The impact of the full shift is conservatively assigned as the estimate of the associated systematic uncertainty. The identification efficiency of the tight selection for unconverted (converted) photons is about 85% (90%) for transverse energies of 25 GeV, and asymptotically reaches a value of 95% (98%) for $E_{\mathrm{T}} > 200$ GeV.

To further reduce the background from jets an isolation requirement is imposed on photon candidates. The analysis makes use of the calorimeter isolation transverse energy $E_{\mathrm{T}}^{\mathrm{iso}}$ defined as the sum of transverse energies of the positive-energy topological clusters [32] within a cone of size $\Delta R = 0.4$ around the photon candidate. The core of the photon shower is excluded, and $E_{\mathrm{T}}^{\mathrm{iso}}$ is corrected for the leakage of the photon shower into the isolation cone. The contributions from the underlying event and pileup are subtracted using the technique proposed in Ref. [33] and implemented as described in Ref. [34]. An additional criterion based on the track isolation transverse momentum is imposed. The track isolation transverse momentum $p_{\mathrm{T}}^{\mathrm{iso}}$ is defined as the scalar sum of the p_{T} of the tracks from the primary vertex with $p_{\mathrm{T}} > 1$ GeV in a $\Delta R = 0.2$ cone around the photon candidate. In events with two selected photon candidates, the pileup dependence of the track isolation transverse momentum is reduced by selecting only tracks consistent with originating from the diphoton production vertex. The selection of the production vertex is discussed below. Tracks associated with photon conversions are excluded from the track isolation transverse momentum.

Diphoton events are initially selected by requiring the presence of at least two photon candidates, satisfying loose identification criteria matching those used to trigger the events, in the fiducial region of the EM calorimeter defined by $|\eta| < 2.37$, excluding the transition region between the barrel and the end-cap calorimeters ($1.37 \leq |\eta| < 1.52$). Photon candidates in this fiducial region are ordered according to their E_{T}, and the first two are considered for further selection if the transverse energy of the leading (subleading) candidate is larger than 40 (30) GeV. The diphoton production vertex is selected from the reconstructed collision vertices using a neural network algorithm. For each vertex the algorithm takes the following inputs: the combined z-position of the intersections of the extrapolated photon trajectories with the beam axis; the sum of the squared transverse momenta $\sum p_{\mathrm{T}}^2$ and the scalar sum of the transverse momenta $\sum p_{\mathrm{T}}$

of the tracks associated with the vertex; the difference in azimuthal angle $\Delta\phi$ between the direction defined by the vector sum of the track momenta and that of the diphoton system. The trajectory of each photon is measured using the longitudinal segmentation of the EM calorimeter and a constraint from the average collision point of the proton beams. For converted photons, the position of the conversion vertex is also used if tracks from the conversion have hits in the silicon detectors. The reconstructed primary vertex that yields the highest output value of the discriminant is selected. The selection of the diphoton production vertex is validated using $Z \to e^+e^-$ events in data and simulation by treating the electron cluster as an unconverted photon candidate [35]. The simulation is found to accurately describe the efficiency measured in data. The efficiency to select a diphoton vertex within 0.3 mm of the production vertex is greater than 95% in events with five or fewer reconstructed primary vertices, and approaches about 80% for events with more than 23 reconstructed primary vertices.

The selected vertex is used to determine the opening angle of the two photons, employed to compute the diphoton invariant mass. The diphoton invariant mass, $m_{\gamma\gamma}$, is evaluated using the leading photon and subleading photon calibrated energies measured in the calorimeter, the azimuthal angle and the pseudorapidity separations between the photons determined from their positions in the calorimeter and the position of the reconstructed diphoton vertex. The diphoton invariant mass resolution, as measured by the σ_{CB} parameter (see Section 4 for details), increases approximatively linearly with $m_{\gamma\gamma}$, ranging from about 2 GeV at $m_{\gamma\gamma} \sim 200$ GeV to about 13 GeV at $m_{\gamma\gamma} \sim 2$ TeV.

6 Event selection

Diphoton events are initially selected following the procedure described in Section 5, and the photon candidates in the selected pairs are additionally required to pass the tight identification criteria. Following the approach used in the Run-1 analysis [13], the leading and subleading photon candidates are then required to satisfy the conditions $E_{\mathrm{T}}^{\gamma_1}/m_{\gamma\gamma} > 0.4$ and $E_{\mathrm{T}}^{\gamma_2}/m_{\gamma\gamma} > 0.3$. For the optimization of these relative selections, a measure of the significance of the signal over the prompt diphoton background is defined. The selections are optimized by maximizing the ratio of the expected significances[4] obtained with the stricter relative selections and with the initial E_{T} selections discussed in Section 3. The optimized relative E_{T} cuts improve the significance by more than 10% for a resonance mass of 200 GeV, and by more than 20% for masses larger than 600 GeV.

The isolation requirement imposed on the photon candidates in the selected pairs is similarly optimized, by maximizing the ratio of the expected significances obtained with and without the isolation criterion. In this case, since the isolation requirement has almost no impact on the irreducible diphoton background, but mostly contributes to reduce the γ-jet and jet-jet reducible components, the optimization procedure uses a mixture of $\gamma\gamma$ and γ-jet Sherpa simulated samples as background, weighted by their respective cross sections. The largest expected relative significance is obtained with a combination of tight selections on the calorimetric isolation transverse energy ($E_{\mathrm{T}}^{\mathrm{iso}} < 0.022 \times E_{\mathrm{T}}^{\gamma} + 2.45$ GeV) and the track isolation transverse momentum ($p_{\mathrm{T}}^{\mathrm{iso}} < 0.05 \times E_{\mathrm{T}}^{\gamma}$). The chosen isolation criteria bring a relative significance improvement exceeding 20% for a resonance mass larger than 600 GeV. Its efficiency ranges from more than 80% for a ggF signal with a mass of 200 GeV, to more than 90% for masses larger than 800 GeV.

[4] The significance of a given selection is calculated as the ratio between the corresponding signal efficiency to the square root of the background efficiency. The ratio of expected significances is independent of the number of signal events, thus no assumption on the signal production cross section is made.

The average $\gamma\gamma$ purity of the diphoton candidate sample selected with the criteria discussed above, as measured with the data-driven method as in Ref. [36], exceeds 90%.

When considering a scalar boson produced via gluon fusion, the total signal selection efficiency of the diphoton requirements discussed above ranges from about 30% for a resonance mass of 200 GeV to more than 40% for masses larger than 600 GeV. The efficiency is larger (ranging from 30% to 45%) for a scalar boson produced via VBF, and smaller (25% to 35%) if ttH production is considered. These differences mainly arise from the kinematic properties of the decay photons when various production modes are considered, and from the differences in jet activity between the different production modes.

If no signal is observed, the analysis sets a limit on the fiducial production cross section times the branching fraction into diphotons $\sigma_{\text{fiducial}} \times \text{BR}(X \to \gamma\gamma)$ as a function of the resonance mass m_X. In order to compute the fiducial cross-section, the number of measured signal events in data must be corrected for the reconstruction, identification and selection efficiencies. A correction factor C_X is defined from simulation as the ratio between the number of reconstructed signal events passing the analysis cuts and the number of signal events at the particle-level generated within a chosen fiducial volume. The particle-level includes all generated particles with a mean lifetime of at least 10 ps. The fiducial volume is chosen to permit a measurement that is independent of the resonance production mode and the final state, i.e. by selecting all events containing two reconstructed photons having similar isolation, identification and reconstruction efficiencies. The definition of the fiducial volume is obtained using simulated samples of a scalar boson produced via ggF, VBF, WH, ZH and ttH. The different production modes are chosen to cover a large variety of possible final states: resonance produced alone, or with associated bosons or additional jets, and within a large kinematic range and variations in how isolated the signal photons are.

The kinematic cuts used to define the fiducial volume mimic those used at the reconstruction level: both photons must be within $|\eta^{\gamma}_{\text{true}}| < 2.37$, although the transition region between the barrel and the end-cap calorimeters $1.37 < |\eta^{\gamma}_{\text{true}}| < 1.52$ is not removed. The transverse energies for the leading and subleading photons are required to be larger than 25 GeV, with additional mass-dependent cuts $E^{\gamma_1}_{\text{T true}} > 0.4\, m^{\text{true}}_{\gamma\gamma}$ and $E^{\gamma_2}_{\text{T true}} > 0.3\, m^{\text{true}}_{\gamma\gamma}$. The difference in signal selection efficiency associated to the different production modes is mitigated by adding a selection on the particle isolation transverse energy $E^{\text{iso}}_{\text{T true}} < 0.05 \times E^{\gamma}_{\text{T true}} + 6$ GeV to the fiducial volume definition. The particle isolation transverse energy is defined as the transverse energy of the vector sum of all stable particles, except muons and neutrinos, found within a $\Delta R = 0.4$ cone around the photon. Within the fiducial volume the total signal efficiency of the diphoton selections ranges from about 55% for a resonance mass of 200 GeV to more than 70% for masses larger than 600 GeV. The difference when considering alternative production modes is about 3% over the considered mass range. The C_X factors used to compute the limit on $\sigma_{\text{fiducial}} \times \text{BR}(X \to \gamma\gamma)$ are parameterized as a function of m_X from the values obtained from the ggF samples. The maximum difference between these values and those corresponding to the other production modes is used as a systematic uncertainty.

7 Signal and background modeling

Analytical descriptions of the signal-plus-background distributions are fitted to the measured $m_{\gamma\gamma}$ spectrum to determine the signal and background yields.

The expected invariant mass distribution of the scalar resonance signal is modeled with a double-sided Crystal Ball function (DSCB, see Section 4) in the mass range [200–2000] GeV, determined from fully

simulated ggF samples. When considering the NWA samples, the width of the DSCB Gaussian core σ_{CB} (Eq. (1)) parameterizes the effect of the experimental invariant mass resolution on the reconstructed $m_{\gamma\gamma}$ distribution, dominated by the photon energy resolution, since for those samples the effect of the natural width of the resonance is negligible with respect to the detector resolution. When considering resonances with larger natural width, simulated as discussed in Section 4, the reconstructed line-shapes are still well described by DSCB functions, but the function parameters effectively parameterize the combined effects of the theoretical line-shape and of the detector response.

Polynomial parameterizations of the signal shape parameters as a function of the resonance mass are obtained from a simultaneous fit to all the generated signal mass points. The signal shape parameters extracted from ggF samples are compared to those from the VBF, WH, ZH and ttH production modes. The bias on the fitted signal yield due to using the ggF shape is found to be negligible.

For a large-width resonance, the evolution of the DSCB parameters (Eq. (1)) for increasing resonance width is parameterized as a function of α. The parameterization is prepared up to $\alpha = 25\%$, even if the search is extended only to the range $\alpha \in [1 - 10]\%$, where the approximate description discussed in Section 4 has been validated.

A data-driven approach is used to estimate the continuous background contribution to the $m_{\gamma\gamma}$ spectrum. The background is modeled by a smooth functional form that models the entire measured $m_{\gamma\gamma}$ spectrum, thus improving upon what was done in the Run-1 analysis [13]. A family of functional forms, adapted from one of those used by searches for new physics signatures in multi-jet final states [37], is chosen:

$$f_{(k)}(x; b, \{a_k\}) = (1 - x^{1/3})^b \, x^{\sum_{j=0}^{k} a_j (\log x)^j} , \tag{2}$$

where $x = \frac{m_{\gamma\gamma}}{\sqrt{s}}$. The preliminary validation of the possible functional forms is performed using the background diphoton MC samples and a γ-jet enriched data sample. The simplest functional version, corresponding to $k = 0$, is already well suited to describe the background shape:

$$f_0(x; b, a_0) = (1 - x^{1/3})^b \, x^{a_0} . \tag{3}$$

The determination of the analytical form of the continuum background and the corresponding uncertainties follow the method detailed in Ref. [3]. The bias on the fitted signal yield induced by a given functional form ("spurious signal") is required to be smaller than a fifth of the statistical uncertainty on the fitted signal yield (obtained with the same functional form). This bias is estimated using a large background-only MC diphoton sample and is accounted for by a mass-dependent uncertainty. The functional form described by Eq. (2) is tested for $k = 0, 1, 2$, and in all configurations it satisfies the criterion for values of the resonance mass ranging from 200 GeV to 3 TeV, with the signal-plus-background fit starting from $m_{\gamma\gamma} = 150$ GeV.

The possibility of needing more degrees of freedom to account for unexpected properties of the data $m_{\gamma\gamma}$ spectrum is considered. In order to decide whether a function with increased complexity is needed to describe the data properties, an F-test [38] is performed. Two background-only fits, using the simplest validated function and a more complex version using an increased k value, are performed on the selected data, binned according to the expected number of background diphoton events. A test statistic F is computed from the resulting χ^2 values, and its probability is compared with that expected from a Fisher distribution with the corresponding number of degrees of freedom. The hypothesis that the additional degree of freedom is useless is rejected if $P(F' \geq F) < 0.05$. The tests do not indicate a need for additional degrees of freedom with respect to the simplest function ($k = 0$).

8 Statistical treatment

The numbers of signal and background events are obtained from unbinned maximum likelihood fits of the $m_{\gamma\gamma}$ distribution of the selected events, for m_X hypotheses in the NWA analysis, or for (m_X, α) pairs, when the presence of a resonance with large natural width is probed. Every fit allows for a single signal component. The whole mass spectrum is used for all probed mass hypotheses. The bias induced on the background fit by the presence of a signal with a mass different from the probed one is measured in simulation and found to be negligible.

A local p-value (p_0) for the background-only hypothesis is calculated using the asymptotic approximation [39]. The uncapped p-value definition is used, so that $p_0 = 0.5$ corresponds to no signal, $p_0 < 0.5$ to positive signal, and $p_0 > 0.5$ to negative signal.

Global significance values are computed accounting for the look-elsewhere-effect (LEE) using the method of Ref. [40], based on the number of positive crossings of the 2σ significance level in the region $m_X \in [200 - 2000]$ GeV. When simultaneously probing for alternative resonance mass and width combinations, the LEE is estimated by scanning the (m_X, α) search plane (2-dimensional LEE) in the region $m_X \in [200 - 2000]$ GeV and $\alpha \in [1 - 10]\%$. The local p-value is based on scanning the $q_0(m_X, \alpha)$ test statistic [39]:

$$q_0(m_X, \alpha) = -2 \log \frac{L(0, m_X, \alpha, \hat{\hat{\nu}})}{L(\hat{\sigma}, m_X, \alpha, \hat{\nu})}, \tag{4}$$

where the values of the parameters marked with the hat superscript are chosen to unconditionally maximize the likelihood, while the value with a double hat is chosen to maximize the likelihood with the fiducial cross-section parameter σ fixed to 0.

The distribution of the maximum local significance $u = \max\left(q_0(m_X, \alpha)\right)$ was studied in Ref. [41]. The global p-value is given by:

$$p_{\text{global}} \approx E[\phi(A_u)] = p_0 + e^{-u/2}(N_1 + \sqrt{u}N_2), \tag{5}$$

where N_1 and N_2 are coefficients that are estimated by calculating the average Euler characteristic with a set of 20 background pseudo-experiments corresponding to the levels $u = 0, 1$.

The expected and observed 95% CL exclusion limits are computed using the asymptotic approximation [39]. Cross-checks using sampling distributions generated using pseudo-experiments are performed for a few mass points.

9 Systematic uncertainties

Systematic uncertainties are accounted for by nuisance parameters in the likelihood functions of the background-only and signal-plus-background fits.

Calibration factors to the energy scale of photons in 13 TeV data are extracted from 8 TeV $Z \to e^+e^-$ decays [31], hence additional systematic uncertainties on the energy scale and resolution are introduced to cover the different conditions between the 2012 and 2015 data taking periods. The increase in photon energy scale uncertainty is largely due to the changes in the LAr calorimeter operating conditions, as well as the updated object reconstruction procedure and detector layout. For the photon energy resolution, the smearing corrections extracted from $Z \to e^+e^-$ events are assigned an additional uncertainty based on a

comparison of simulated $Z \to e^+e^-$ samples in the 8 TeV and 13 TeV simulation setup, which differ in particular by the addition of the IBL in the 13 TeV detector.

The uncertainty on the photon energy resolution affects the width of the DSCB function used in the NWA signal model with an asymmetric uncertainty of $^{+55\%}_{-20\%}$ for a resonance mass of 200 GeV, rising to $^{+110\%}_{-40\%}$ for a mass of 2 TeV. The effects on the fitted signal yields of the pileup modeling, of the photon energy scale uncertainty, of the photon identification and isolation, and of the differences induced on the signal modeling by the alternative production modes are studied, and all are found to be negligible.

The potential bias on the signal yield due to the use of the background functional form described by Eq. (2) with $k = 0$ ranges from 2 to 10^{-3} events in the [200-2000] GeV mass range when a NWA signal is considered. When a large-width resonance is probed for, this uncertainty varies in the same mass range from 4 to $7 \cdot 10^{-3}$ events for $\alpha = 6\%$, and from 7 to 10^{-2} events for $\alpha = 10\%$.

The statistical uncertainty on the background component of the fits induces a mass-dependent uncertainty on the fitted signal yields. This uncertainty is maximal in absence of signal, when it amounts to about 50% of the total uncertainty on the fitted signal yield for a probed resonance mass of 200 GeV, reducing to about 20% for a probed mass of 2 TeV.

Effects of the photon energy scale and resolution uncertainties on the correction factors C_X through migrations of detector-level events into and out of the defined fiducial volume are evaluated and found to be negligible. Uncertainties on the trigger efficiency, photon identification efficiency, and photon isolation efficiencies also change the number of detector-level events by a uniform shift of the normalization. The trigger uncertainty is estimated by comparing the efficiency of the trigger selection in the MC simulation and the efficiency observed in data as a function of the photon E_{T}. The absolute difference between these two measurements is taken as the uncertainty. The uncertainty associated to the modeling of the efficiency of selecting the primary vertex, used to correct the E_{T} of the photon candidates, is found to be negligible. The uncertainty induced on the C_X factors by the uncertainty of the photon identification efficiency is determined by comparing the efficiency derived after applying MC-to-data shifts to the calorimeter shower shapes in simulation, to the efficiency in simulation derived before these corrections are applied. It varies from 2% to 3% in the [200–2000] GeV mass range for a NWA signal. The isolation efficiency uncertainty is affected by both the calorimeter and charged-particle tracking components of the requirement. A MC-to-data shift is applied to the calorimeter isolation energy of photons in MC simulation when deriving the correction factors C_X, and the difference from the corresponding nominal correction factor is taken as the associated uncertainty. A similar procedure is applied to the track isolation. The C_X uncertainty associated to the isolation criterion ranges from 1% to 4.1% in the [200–2000] GeV mass range for a NWA signal. The largest difference between the C_X factor corresponding to a ggF signal and the alternative production modes is accounted for as a systematic uncertainty. It is at most 3.1% for all values of the resonance mass considered in the fiducial volume of interest for a NWA signal.

The measurement of the integrated luminosity has an uncertainty of 5%. It is derived, following a methodology similar to that detailed in Ref. [42], from a preliminary calibration of the luminosity scale using a pair of van der Meer scans performed in June 2015.

Table 1 shows all uncertainty contributions when considering the NWA signal model. All uncertainty contributions affecting the correction factors C_X are added in quadrature and are treated as single uncertainty source.

Source	Uncertainty
Background modeling $^{\circ\bullet}$	
Spurious signal	$2-10^{-3}$ events, mass-dependent
Background fit	$\leq 50\%$–$\leq 20\%$ of the total signal yield uncertainty, mass- and signal-dependent
Signal modeling $^{\circ\bullet}$	
Photon energy resolution	$^{+[55-110]\%}_{-[20-40]\%}$, mass-dependent
Signal yield $^{\bullet}$	
Luminosity	$\pm 5\%$
Trigger	$\pm 0.63\%$
C_X factors $^{\bullet}$	
Photon identification	$\pm(3$–$2)\%$, mass-dependent
Photon isolation	$\pm(4.1$–$1)\%$, mass-dependent
Production process	$\pm 3.1\%$

Table 1: Summary of the systematic uncertainties in the signal-plus-background likelihood fit when considering the NWA signal model. The $\circ$ symbol denotes categories of uncertainties that affect the local p-value for the background-only hypothesis, while the $\bullet$ symbol denotes uncertainties that impact the limit on $\sigma_{\text{fiducial}} \times \text{BR}(X \to \gamma\gamma)$.

10 Results

Figure 1 shows the diphoton mass spectrum observed in data, with the result of an unbinned background-only fit superimposed. The uncapped local p_0, as obtained by the signal-plus-background likelihood fits under the NWA hypothesis for the signal, is shown in Figure 2. The most significant deviation from the background hypothesis is observed for a mass of about 750 GeV, corresponding to a local significance of 3.6 σ, and to a global significance of 2.0 σ when the LEE taking into account the mass range $m_X \in [200 - 2000]$ GeV is accounted for. The second most significant deviation from the background-only hypothesis is found for a mass of about 1.6 TeV, corresponding to a local significance of 2.8 σ.

In the region around 750 GeV, the NWA fits exhibit a $\sim$1.5 σ pull on the nuisance parameter associated with the photon energy resolution uncertainty, indicating an excess broader than the experimental $m_{\gamma\gamma}$ invariant mass resolution. After this behavior was observed, signal-plus-background fits were also performed assuming a large width for the signal component. The largest deviation from the background-only hypothesis is observed for a mass around 750 GeV and $\alpha \simeq 6\%$, corresponding to a width Γ of about 45 GeV. The local significance increases when allowing the width to vary, as expected. The local (global) significance evaluated for the large width fit is about 0.3 higher than that for the NWA fit, corresponding to 3.9 (2.3) σ. The global significance value is obtained accounting for a 2-dimensional LEE corresponding to the scan range $m_X \in [200 - 2000]$ GeV and $\alpha \in [1 - 10]\%$.[5]

In the excess region, defined as $m_{\gamma\gamma} \in [700, 800]$ GeV, the numbers of fitted signal and background events under both the NWA and large-width hypotheses are about equal.

[5] The stability of the 2-dimensional LEE correction is evaluated by considering a larger scan range for the α parameter. When extending the range to $\alpha \in [1 - 25]\%$ the global significance is only marginally affected, reducing at most by 0.05 with respect to the value obtained considering the $[1 - 10]\%$ range.

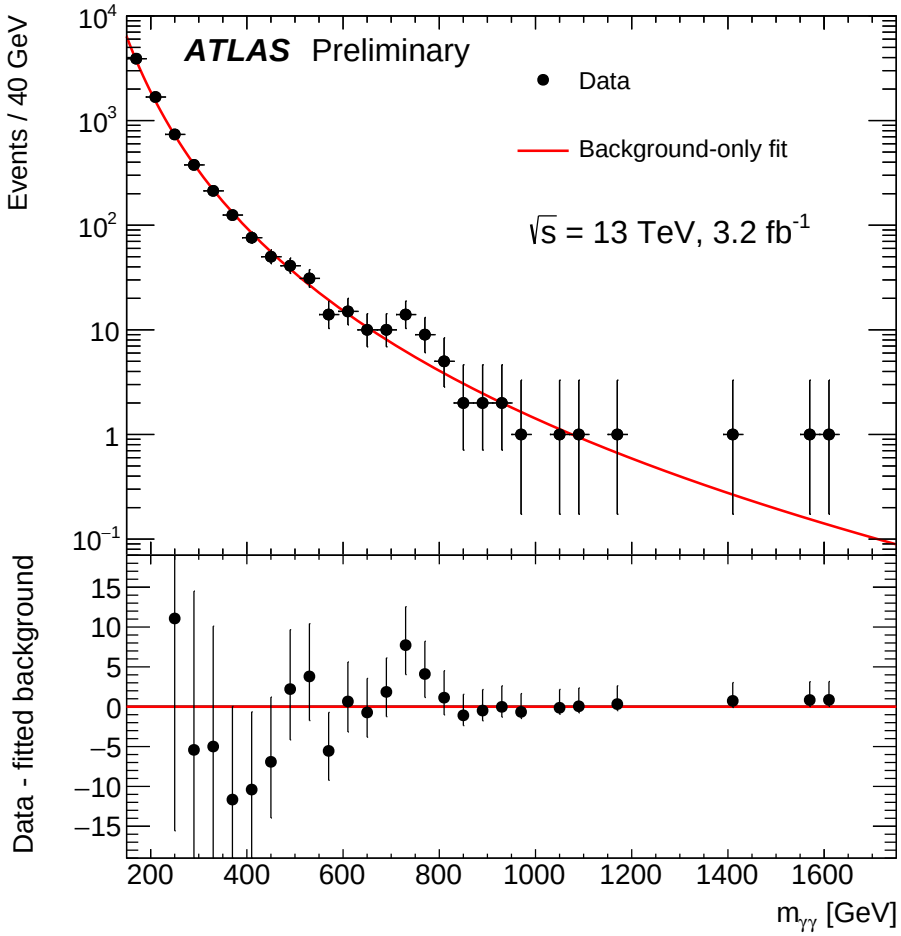

Figure 1: Invariant mass distribution of the selected diphoton events. Residual number of events with respect to the fit result are shown in the bottom pane. The first two bins in the lower pane are outside the vertical plot range.

The events in this region are scrutinized. No detector or reconstruction effect that could explain the larger rate is found, nor any indication of anomalous background contamination. The kinematic properties of these events are studied with respect to those of events populating the invariant mass regions above and below the excess, and no significant difference is observed.

The Run-1 analysis presented in Ref. [13] is extended to invariant masses larger than 600 GeV by using the new background modeling techniques presented in this note (cf. Section 7). The compatibility between the results obtained with the 8 TeV and 13 TeV datasets is estimated under the NWA hypothesis and assuming a large-width resonance with $\alpha = 6\%$, using the best fit value of the ratio of cross sections. For an s-channel gluon-initiated process, the parton-luminosity ratio is expected to be 4.7 [43]. Under those assumptions, the results obtained with the two datasets are found to be compatible within 2.2 and 1.4 standard deviations for the two width hypotheses respectively.

The 95% CL expected and observed upper limits on $\sigma_{\text{fiducial}} \times \text{BR}(X \to \gamma\gamma)$, corresponding to the fiducial volume defined in Section 6, are computed using the CL_s technique [39, 44] for a scalar resonance with narrow width as a function of the mass hypothesis m_X, and are presented in Figure 3. The larger diphoton rate in the mass region around 750 GeV is translated to a higher-than-expected cross section limit at the

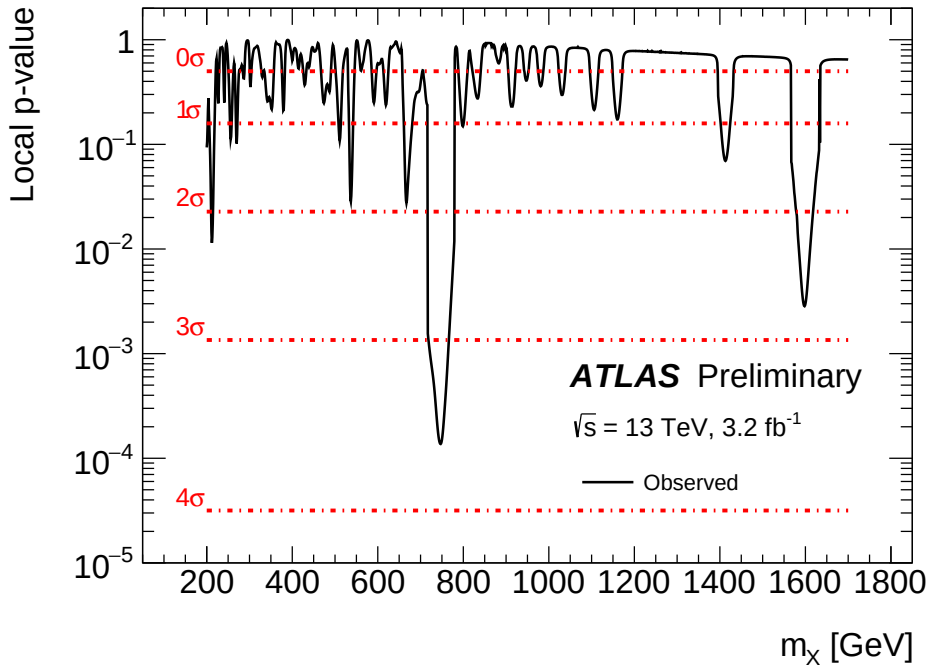

Figure 2: p-value for the background-only hypothesis p_0 as a function of the mass m_X of a probed NWA resonance signal.

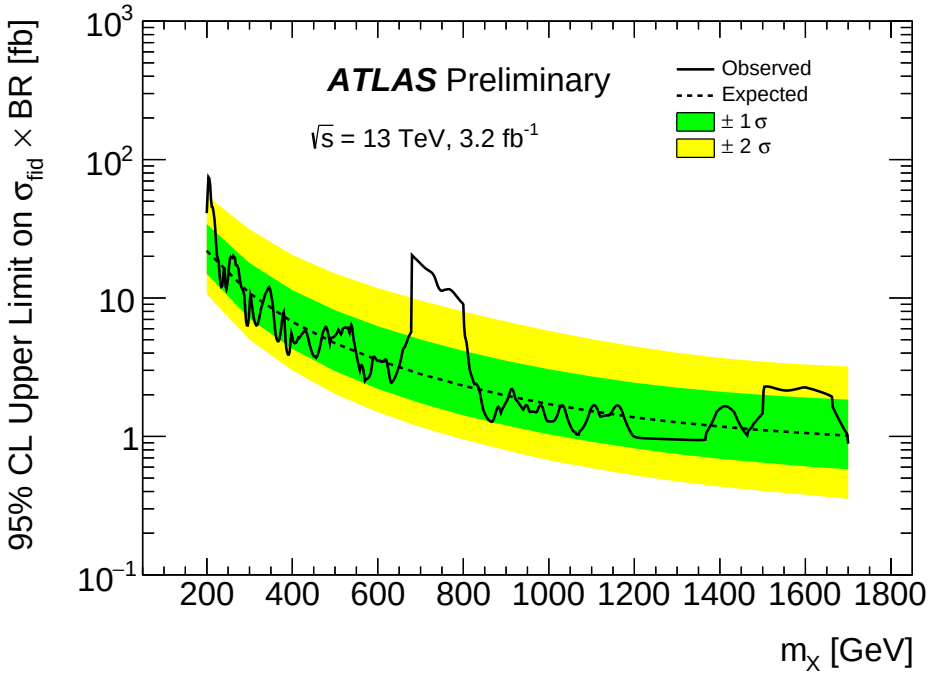

Figure 3: Expected and observed upper limits on $\sigma_{\text{fiducial}} \times \text{BR}(X \to \gamma\gamma)$ expressed at 95% CL, as a function of the assumed value of the narrow-width scalar resonance mass.

same area. The sharp rise and fall of the limit values at the boundaries of this region is due to the fits pulling the nuisance parameter associated to the photon energy resolution.

The validity of the limit on $\sigma_{\text{fiducial}} \times \text{BR}(X \to \gamma\gamma)$ for resonances with non-negligible natural width is estimated by evaluating the bias on the number of fitted signal events from a large-width resonance when a NWA signal parameterization is used. The test is performed by injecting a number of large-width signal events corresponding to the expected NWA $\sigma_{\text{fiducial}} \times \text{BR}(X \to \gamma\gamma)$ limit. A bias on the number of fitted signal events obtained using the NWA signal parameterization, which systematically underestimates the yields from a large-width signal, is found to be smaller than 10% (20%) for a natural width given by $\alpha = 0.4\%$ ($\alpha = 1.4\%$).

11 Conclusions

A search is presented for new scalar resonances decaying to a pair of photons, such as those expected in models with an extended Higgs sector, using a sample of 3.2 fb^{-1} of pp collisions at $\sqrt{s} = 13$ TeV recorded in 2015 with the ATLAS detector at the Large Hadron Collider. The analysis studies the $m_{\gamma\gamma}$ region above 150 GeV, probing resonance masses from 200 GeV.

The largest deviation from the background-only hypothesis is found in a broad region around 750 GeV, with a global significance of about 2 standard deviations. The properties of the events in this region are found to be compatible with those in the invariant mass regions above and below the excess.

An upper limit at 95% CL is reported on the fiducial production cross section of a narrow scalar boson times its decay branching ratio into two photons, for masses ranging from 200 GeV to 1.7 TeV.

References

[1] ATLAS Collaboration, *The ATLAS experiment at the CERN Large Hadron Collider*, JINST **3** (2008) S08003.

[2] ATLAS Collaboration, *ATLAS Insertable B-Layer Technical Design Report*, CERN-LHCC-2010-013. ATLAS-TDR-19 (2010), URL: https://cds.cern.ch/record/1291633.

[3] ATLAS Collaboration, *Observation of a new particle in the search for the Standard Model Higgs boson with the ATLAS detector at the LHC*, Phys. Lett. B **716** (2012) 1, arXiv: 1207.7214 [hep-ex].

[4] CMS Collaboration, *Observation of a new boson at a mass of 125 GeV with the CMS experiment at the LHC*, Phys. Lett. B **716** (2012) 30, arXiv: 1207.7235 [hep-ex].

[5] ATLAS and CMS Collaborations, *Combined Measurement of the Higgs Boson Mass in pp Collisions at $\sqrt{s} = 7$ and 8 TeV with the ATLAS and CMS Experiments*, Phys. Rev. Lett. **114** (2015) 191803, arXiv: 1503.07589 [hep-ex].

[6] A. Hill and J. J. van der Bij, *Strongly interacting singlet - doublet Higgs model*, Phys. Rev. D **36** (1987) 3463.

[7] M. J. G. Veltman and F. J. Yndurain, *Radiative correction to WW scattering*, Nucl. Phys. B **325** (1989) 1.

[8] T. Binoth and J. J. van der Bij, *Influence of strongly coupled, hidden scalars on Higgs signals*, Z. Phys. C **75** (1997) 17, arXiv: hep-ph/9608245 [hep-ph].

[9] R. Schabinger and J. D. Wells, *A Minimal spontaneously broken hidden sector and its impact on Higgs boson physics at the large hadron collider*, Phys. Rev. D **72** (2005) 093007, arXiv: hep-ph/0509209 [hep-ph].

[10] B. Patt and F. Wilczek, *Higgs-field portal into hidden sectors* (2006), arXiv: hep-ph/0605188 [hep-ph].

[11] G. M. Pruna and T. Robens, *Higgs singlet extension parameter space in the light of the LHC discovery*, Phys. Rev. D **88** (2013) 115012, arXiv: 1303.1150 [hep-ph].

[12] T. D. Lee, *A theory of spontaneous T violation*, Phys. Rev. D **8** (1973) 1226.

[13] ATLAS Collaboration, *Search for scalar diphoton resonances in the mass range* $65 - 600$ *GeV with the ATLAS detector in pp collision data at* $\sqrt{s} = 8\,TeV$, Phys. Rev. Lett. **113** (2014) 171801, arXiv: 1407.6583 [hep-ex].

[14] CMS Collaboration, *Search for diphoton resonances in the mass range from 150 to 850 GeV in pp collisions at* $\sqrt{s} = 8$ *TeV*, Phys. Lett. B **750** (2015) 494, arXiv: 1506.02301 [hep-ex].

[15] ATLAS Collaboration, *The ATLAS simulation infrastructure*, Eur. Phys. J. **C70** (2010) 823, arXiv: 1005.4568 [physics.ins-det].

[16] S. Agostinelli et al., *GEANT4: A simulation toolkit*, Nucl. Instrum. Meth. **A506** (2003) 250.

[17] T. Sjöstrand, S. Mrenna, and P. Z. Skands, *A Brief Introduction to PYTHIA 8.1*, Comput. Phys. Commun. **178** (2008) 852, arXiv: 0710.3820 [hep-ph].

[18] S. Alioli et al., *A general framework for implementing NLO calculations in shower Monte Carlo programs: the POWHEG BOX*, J. High Energy Phys. 06 (2010) 043, arXiv: 1002.2581 [hep-ph].

[19] E. Bagnaschi et al., *Higgs production via gluon fusion in the POWHEG approach in the SM and in the MSSM*, J. High Energy Phys. 02 (2012) 088, arXiv: 1111.2854 [hep-ph].

[20] P. Nason and C. Oleari, *NLO Higgs boson production via vector-boson fusion matched with shower in POWHEG*, JHEP **1002** (2010) 037, arXiv: 0911.5299 [hep-ph].

[21] ATLAS Collaboration, *Measurement of the Z boson transverse momentum distribution in pp collisions at* $\sqrt{s} = 7$ *TeV with the ATLAS detector*, J. High Energy Phys. **2014** (2014) 55, arXiv: 1406.3660 [hep-ex].

[22] ATLAS Collaboration, *ATLAS Pythia 8 tunes to* 7 *TeV data*, ATL-PHYS-PUB-2014-021 (2014), URL: http://cdsweb.cern.ch/record/1966419.

[23] H.-L. Lai et al., *New parton distributions for collider physics*, Phys. Rev. D **82** (2010) 074024, arXiv: 1007.2241 [hep-ph].

[24] P. Nason, *A new method for combining NLO QCD with shower Monte Carlo algorithms*, J. High Energy Phys. 11 (2004) 040, arXiv: hep-ph/0409146 [hep-ph].

[25] S. Frixione, P. Nason, and C. Oleari,
Matching NLO QCD computations with Parton Shower simulations: the POWHEG method,
J. High Energy Phys. 11 (2007) 070, arXiv: 0709.2092 [hep-ph].

[26] J. Pumplin et al.,
New generation of parton distributions with uncertainties from global QCD analysis,
JHEP **07** (2002) 012, arXiv: hep-ph/0201195 [hep-ph].

[27] S. Alioli et al., *NLO Higgs boson production via gluon fusion matched with shower in POWHEG*,
JHEP **0904** (2009) 002, arXiv: 0812.0578 [hep-ph].

[28] T. Gleisberg et al., *Event generation with SHERPA 1.1*, J. High Energy Phys. **0902** (2009) 007,
arXiv: 0811.4622 [hep-ph].

[29] T. Binoth et al.,
A full next-to-leading order study of direct photon pair production in hadronic collisions,
Eur. Phys. J. C **16** (2000) 311, arXiv: hep-ph/9911340 [hep-ph].

[30] ATLAS Collaboration, *Expected photon performance in the ATLAS experiment*,
ATL-PHYS-PUB-2011-007 (2011), URL: http://cdsweb.cern.ch/record/1345329.

[31] ATLAS Collaboration,
Electron and photon energy calibration with the ATLAS detector using LHC Run 1 data,
Eur. Phys. J. **C74**.10 (2014) 3071, arXiv: 1407.5063 [hep-ex].

[32] W. Lampl et al., *Calorimeter Clustering Algorithms: Description and Performance*,
ATL-LARG-PUB-2008-002 (2008), http://cdsweb.cern.ch/record/1099735.

[33] M. Cacciari, G. P. Salam, and G. Soyez, *The Catchment Area of Jets*,
J. High Energy Phys. **04** (2008) 005, arXiv: 0802.1188 [hep-ph].

[34] ATLAS Collaboration, *Measurement of the isolated di-photon cross-section in pp collisions at $\sqrt{s} = 7$ TeV with the ATLAS detector*, Phys.Rev. **D85** (2012) 012003,
arXiv: 1107.0581 [hep-ex].

[35] ATLAS Collaboration, *Measurement of the Higgs boson production cross section at 7, 8 and 13 TeV center-of-mass energies in the $H \to \gamma\gamma$ channel with the ATLAS detector.*,
ATLAS-CONF-2015-060 (2015), URL: https://atlas.web.cern.ch/Atlas/GROUPS/PHYSICS/CONFNOTES/ATLAS-CONF-2015-060.

[36] ATLAS Collaboration, *Measurement of isolated-photon pair production in pp collisions at $\sqrt{s} = 7$ TeV with the ATLAS detector*, J. High Energy Phys. **01** (2013) 086,
arXiv: 1211.1913 [hep-ex].

[37] ATLAS Collaboration, *Search for New Particles in Two-Jet Final States in 7 TeV Proton-Proton Collisions with the ATLAS Detector at the LHC*, Phys. Rev. Lett. **105** (2010) 161801,
arXiv: 1008.2461 [hep-ex].

[38] G. Snecdecor and W. Cochran, *Statistical Methods*, vol. 276, Wiley, 1991, ISBN: 9780813815619.

[39] G. Cowan et al., *Asymptotic formulae for likelihood-based tests of new physics*,
Eur. Phys. J. C **71** (2011) 1554, [Erratum: Eur. Phys. J.C73,2501(2013)],
arXiv: 1007.1727 [physics.data-an].

[40] E. Gross and O. Vitells, *Trial factors or the look elsewhere effect in high energy physics*,
Eur. Phys. J. C **70** (2010) 525, arXiv: 1005.1891 [physics.data-an].

[41] O. Vitells and E. Gross, *Estimating the significance of a signal in a multi-dimensional search*, Astropart. Phys. **35** (2011) 230, arXiv: 1105.4355 [astro-ph.IM].

[42] ATLAS Collaboration, *Improved luminosity determination in pp collisions at sqrt(s) = 7 TeV using the ATLAS detector at the LHC*, Eur. Phys. J. **C73**.8 (2013) 2518, arXiv: 1302.4393 [hep-ex].

[43] A. Martin et al., *Parton distributions for the LHC*, Eur. Phys. J. C **63** (2009) 189, arXiv: 0901.0002 [hep-ph].

[44] A. L. Read, *Presentation of search results: The CL(s) technique*, J. Phys. **G28** (2002) 2693.